Measurement-Based Sparsity-Promoting Optimal Control of Line Flows

Abdullah Al-Digs , *Student Member, IEEE*, Sairaj V. Dhople , *Member, IEEE*,
and Yu Christine Chen , *Member, IEEE*

Abstract—This paper proposes an optimal strategy for regulating active-power flows in electric power systems based on sparsity-promoting linear–quadratic–Gaussian (LQG) control. The proposed method relies on the mapping of nodal active- and reactive-power injections to line flows, which are obtained via a measurement-based approach. Building on this, we outline a combined sparsity-promoting linear–quadratic regulator and Kalman-filter design. The optimal controller sparsity is identified using the alternating direction method of multipliers, which strikes a balance between feedback controller sparsity and the closed-loop dynamic performance. With this, we optimally dispatch generators and controllable loads to achieve desired line flows while ensuring zero steady-state frequency offset. We demonstrate the utility of the proposed LQG controller via a representative congestion-management application deployed on the New England 10-machine 39-bus test system.

Index Terms—Alternating direction method of multipliers (ADMM), injection shift factors, linear-quadratic-Gaussian control, line-flow control, optimization, sparsity-promoting control.

I. INTRODUCTION

WITH rapidly growing global electricity demand, there is impetus to expand existing transmission infrastructure, but this may be hindered by economic and environmental constraints [1], and in turn, transmission lines may become overloaded (i.e., operate above their thermal limits) or nearly so [2]. Thus, it is necessary to develop effective line-flow control methods that optimally utilize existing and expected infrastructure resources, such as conventional power plants, controllable loads, and distributed energy resources[1] (DERs), while maintaining reliable and secure system operation. In such a setting, dispatchable loads and DERs, e.g., rooftop solar photovoltaics and energy storage devices, provide the necessary flexibility as active-power injection control inputs to achieve desired line active-power flows and system frequency in a timely fashion. However, controlling a large number of geographically dispersed loads and injections in a centralized manner requires sizeable communication networks and wide-area actuation capabilities. To effectively regulate line flows in large-scale electric power systems, local-area decision making offers a practical and attractive alternative with several advantages, including (i) active participation of consumers via, e.g., demand response, (ii) optimized utilization of existing assets, and (iii) accommodating and utilizing all generation and storage technologies [3], [4]. To this end, we propose a strategy to regulate transmission-line active-power flows and system frequency to desired reference values using a sparsity-promoting linear-quadratic-Gaussian (LQG) controller.

Line-flow control is potentially useful in a variety of operational tasks, such as congestion management, automatic generation control (AGC), and eliminating redundant loop flows [5], [6]. In this paper, we propose a method that regulates line-flow and system-frequency trajectories to asymptotically converge to their desired reference values, by optimally dispatching active-power injections at electrically nearby buses. The proposed control strategy is novel from several perspectives. First, by leveraging a sparsity-promoting control design, the resulting feedback structure requires only local actuation capabilities to achieve desired line flows. As illustrated via extensive numerical case studies, desired control aims are achieved with sufficient accuracy while the controller synthesis effort is significantly reduced by constructing suitably simplified power-system models. For example, the line-flow dynamical model relies on linear mappings of nodal injections to line active-power flows, and generator dynamics are captured by the swing equation along with a governor. Finally, the injections-to-flows mapping can be obtained by using only real-time measurements without relying on an offline system network model, which enables the controller to be adaptive to system-topology or operating-point changes.

Existing methods to accomplish line-flow control can be categorized as (i) centralized, (ii) distributed, and (iii) decentralized. Centralized line-flow control is performed as part of the AGC system, which maintains scheduled inter-area tie-line flows and ensures that each balancing area serves its own net load [7], [8]. However, this requires a central decision maker and a substantial communication infrastructure. On the other hand, distributed

A. Al-Digs and Y. C. Chen are with the Department of Electrical and Computer Engineering, The University of British Columbia, Vancouver, BC V6T 1Z2, Canada (e-mail: aldigs@ece.ubc.ca; chen@ece.ubc.ca).

S. V. Dhople is with the Department of Electrical and Computer Engineering, University of Minnesota, Minneapolis, MN 55455 USA (e-mail: sdhople@umn.edu).

[1]A list of abbreviated terms used in this paper appears in Appendix A.

consensus-based controllers arrive at actuation decisions collectively. This process may necessitate numerous instances of information exchange amongst nodes in the system, which may result in longer convergence times [9]. Finally, decentralized line-flow control has been realized through hardware-based control using, e.g., distributed static series compensators [10], phase shifting transformers [11], flexible AC transmission system controllers [2], and unified power flow controllers [1]. While these solutions require little to no communication, they necessitate additional infrastructure investment and installing them ubiquitously may be economically prohibitive. Furthermore, they do not adapt to contingencies and system modifications, nor do they guarantee global optimality [12]. Distinct from prior work mentioned above, our proposed control strategy leverages existing resources, requires only local actuation signals, and adapts to potential operating-point and topology changes. This is accomplished by incorporating real-time measurements and dispatching electrically nearby synchronous generators and controllable loads in order to optimally regulate line flows and system frequency.

This paper builds on our preliminary work reported in [13] and provides extensions in several directions. First, in addition to tracking line flows in [13], we incorporate synchronous-machine dynamics into the modelling framework to enable optimal regulation of system frequency. Second, we utilize a measurement-based method to obtain the up-to-date injections-to-flows mapping and illustrate via numerical case studies that, compared to the model-based alternative, the improved controller is adaptive to changes in network topology and system operating point. Additionally, in order to develop a controller that requires only local-area actuation capability, we tailor the continuous-time sparsity-promoting optimal control framework in [14] to our discrete-time problem setting and assess the trade-off between controller sparsity and corresponding dynamic performance. Worth mentioning here are prior efforts that use sparsity-promoting methods for a variety of *other* power-system applications, such as wide-area control [15] and damping inter-area oscillations [16], [17]. A review of additional pertinent applications is available in [18]. Finally, we illustrate the efficacy of the controller via numerical case studies involving the Western Electricity Coordinating Council (WECC) and the New England (NE) test systems.

The remainder of this manuscript is organized as follows. In Section II, we establish mathematical notation and describe the system and pertinent dynamical models. Section III outlines design aspects of the LQG controller to achieve optimal tracking of line active-power flows while maintaining nominal system frequency. The sparsity-promoting optimal control problem and optimization algorithm for its synthesis are outlined in Section IV. In Section V, we demonstrate the utility of the sparsity-promoting optimal controller via case studies involving the WECC and NE test systems. Finally, concluding remarks and directions for future work are provided in Section VI.

II. Preliminaries

This section establishes mathematical notation, describes the power system network, and outlines the mapping of nodal active- and reactive-power injections to line active-power flows. Furthermore, we present the system dynamical models required for controller design.

A. Mathematical Notation

The matrix inverse is denoted by $(\cdot)^{-1}$, transpose by $(\cdot)^{\mathrm{T}}$, trace by $\mathrm{Tr}\{\cdot\}$, and Frobenius norm by $\|\cdot\|_{\mathrm{F}}$. The magnitude of a complex-valued scalar and cardinality of a set are denoted by $|\cdot|$. A diagonal matrix formed with entries of the vector x stacked on the main diagonal is denoted by $\mathrm{diag}(x)$; and $\mathrm{diag}(x/y)$ forms a diagonal matrix with the ith diagonal entry given by x_i/y_i, where x_i and y_i are the ith entries of vectors x and y, respectively. For column vectors $x = [x_1, \ldots, x_M]^{\mathrm{T}}$ and $y = [y_1, \ldots, y_M]^{\mathrm{T}}$, $x \circ y$ denotes the entry-wise product. The spaces of M-dimensional real- and complex-valued column vectors are denoted by $\mathbb{R}^M$ and $\mathbb{C}^M$, respectively; the spaces of $L \times M$ real- and complex-valued matrices are denoted by $\mathbb{R}^{L \times M}$ and $\mathbb{C}^{L \times M}$, respectively. The $N \times N$ identity matrix is denoted by I_N. The standard inner product of matrices A and B is denoted by $\langle A, B \rangle = \mathrm{Tr}(A^{\mathrm{T}}B)$. The M-dimensional vectors with all 0's and 1's are denoted by $\mathbb{0}_M$ and $\mathbb{1}_M$, respectively; e_i denotes a column vector with all 0's except with the ith entry equal to 1, and $e_{ij} := e_i - e_j$. For a vector $\theta = [\theta_1, \ldots, \theta_M]^{\mathrm{T}}$, $\theta_i \in [-\pi, \pi] \ \forall \ i = 1, \ldots, M$, $\cos(\theta) := [\cos(\theta_1), \ldots, \cos(\theta_M)]^{\mathrm{T}}$ and $\sin(\theta) := [\sin(\theta_1), \ldots, \sin(\theta_M)]^{\mathrm{T}}$.

B. Network Description

Consider an AC network with nodes collected in the set $\mathcal{N} = \mathcal{G} \cup \mathcal{L}$, where $\mathcal{G}$ and $\mathcal{L}$ denote the sets of generator and load buses, respectively. Transmission lines (each represented by two directed edges) are collected in the set of edges $\mathcal{E} := \{(m, n)\} \subseteq \mathcal{N} \times \mathcal{N}$. Each transmission line connecting buses m and n is modelled using the lumped-parameter Π-model with series admittance $y_{mn} \in \mathbb{C}$ and shunt admittance $y_{mn}^{\mathrm{sh}} \in \mathbb{C}$. Then, the entry in the mth row and nth column of the network admittance matrix, denoted by Y, is specified as

$$[Y]_{mn} := \begin{cases} y_m + \sum_{(m,k) \in \mathcal{E}} y_{mk}, & \text{if } m = n, \\ -y_{mn}, & \text{if } (m, n) \in \mathcal{E}, \\ 0, & \text{otherwise,} \end{cases} \quad (1)$$

where

$$y_m = g_m + \mathrm{j}b_m := y_{mm} + \sum_{k \in \mathcal{N}_m} y_{mk}^{\mathrm{sh}} \quad (2)$$

denotes the total shunt admittance connected to node m, $\mathcal{N}_m \subseteq \mathcal{N}$ represents the set of neighbours of node m, and $y_{mm} \in \mathbb{C}$ captures any passive shunt elements connected to node m. Let $V_{i,[k]} = |V_{i,[k]}| \angle \theta_{i,[k]} \in \mathbb{C}$ represent the voltage phasor at node i at discrete time instant $k = 0, 1, \ldots$; and let $I_{i,[k]} \in \mathbb{C}$ denote the current injected into node i at time instant k. Furthermore, collect steady-state nodal voltage phasors into the vector $V_{[k]} = [V_{1,[k]}, \ldots, V_{|\mathcal{N}|,[k]}]^{\mathrm{T}}$ and current injections into $I_{[k]} = [I_{1,[k]}, \ldots, I_{|\mathcal{N}|,[k]}]^{\mathrm{T}}$. Then, at time instant k, applying Kirchhoff's current law at each node and stacking them into

matrix-vector form, we get

$$I_{[k]} = Y V_{[k]}. \tag{3}$$

Denote the vector of complex-power nodal injections at time instant k by $S_{[k]} = [S_{1,[k]}, \ldots, S_{|\mathcal{N}|,[k]}]^\mathrm{T} = P_{[k]} + \mathrm{j} Q_{[k]}$, with $P_{[k]} = [P_{1,[k]}, \ldots, P_{|\mathcal{N}|,[k]}]^\mathrm{T}$ and $Q_{[k]} = [Q_{1,[k]}, \ldots, Q_{|\mathcal{N}|,[k]}]^\mathrm{T}$. (By convention, $P_{i,[k]}$ and $Q_{i,[k]}$ are positive for generation and negative for loads.) Then, complex-power nodal injections can be compactly written as

$$S_{[k]} = \mathrm{diag}\left(V_{[k]} \right) I_{[k]}^*. \tag{4}$$

C. Model- and Measurement-based Line-Flow Sensitivities

Recall that our goal is to regulate line active-power flows to desired values by optimally modulating active-power injections. To this end, consider variations in the active power flowing across line (m, n), denoted by $\Delta P_{(m,n),[k]}$, resulting from nodal active-power injections $\Delta P_{[k]} = P_{[k+1]} - P_{[k]}$, which are approximated by

$$\Delta P_{(m,n),[k]} \approx \Phi_{(m,n),[k]} \Delta P_{[k]} + \zeta_{(m,n),[k]}, \tag{5}$$

where $\zeta_{(m,n),[k]}$ represents a *bounded* disturbance due to variations in reactive-power injections and errors in the linear approximation. In practice, $\zeta_{(m,n),[k]}$ is small for transmission-level lines where the active- and reactive-power decoupling assumptions are valid [19]. The injections-to-flow mapping in (5) will be useful to uncover discrete-time line-flow dynamics in Section II-D. The sensitivities $\Phi_{(m,n),[k]}$ can be computed via model- and measurement-based approaches, described below. Note that while they can be computed at each time instant k, in practical implementation, we envision that they would be updated periodically as the operating point sufficiently deviates from the previous one at which they were obtained.

1) Model-Based Sensitivities: Express the current flowing in line $(m, n) \in \mathcal{E}$ at time instant k as

$$I_{(m,n),[k]} = \left(y_{mn} e_{mn}^\mathrm{T} + y_m^\mathrm{sh} e_m^\mathrm{T} \right) Y^{-1} I_{[k]}$$
$$=: (\alpha_{(m,n)}^\mathrm{T} + \mathrm{j}\beta_{(m,n)}^\mathrm{T}) I_{[k]}, \tag{6}$$

where $\alpha_{(m,n)}^\mathrm{T} + \mathrm{j}\beta_{(m,n)}^\mathrm{T} \in \mathbb{C}^{|\mathcal{N}|}$ are the current injection sensitivity factors. Denote, by $S_{(m,n),[k]} = P_{(m,n),[k]} + \mathrm{j}Q_{(m,n),[k]}$, the complex power flowing across line (m, n). We can write

$$S_{(m,n),[k]} = V_{m,[k]} I_{(m,n),[k]}^*. \tag{7}$$

Substituting the current injection sensitivity factors from (6) into (7), and defining $\theta^m := \theta_m \mathbb{1}_{|\mathcal{N}|} - \theta$, we obtain [20]

$$P_{(m,n),[k]} = \Phi_{(m,n),[k]} P_{[k]} + \varepsilon_{(m,n),[k]}, \tag{8}$$

where

$$\Phi_{(m,n),[k]} = |V_m| u_{(m,n)}^\mathrm{T}, \quad \varepsilon_{(m,n),[k]} = -|V_m| v_{(m,n)}^\mathrm{T} Q_{[k]}, \tag{9}$$

with $u_{(m,n)}, v_{(m,n)} \in \mathbb{R}^{|\mathcal{N}|}$ given by

$$u_{(m,n)} = \mathrm{diag}\left(\frac{\cos(\theta^m)}{|V|} \right) \alpha_{(m,n)} + \mathrm{diag}\left(\frac{\sin(\theta^m)}{|V|} \right) \beta_{(m,n)}, \tag{10}$$

$$v_{(m,n)} = \mathrm{diag}\left(\frac{\sin(\theta^m)}{|V|} \right) \alpha_{(m,n)} - \mathrm{diag}\left(\frac{\cos(\theta^m)}{|V|} \right) \beta_{(m,n)}. \tag{11}$$

The expression in (8) reveals the contribution of each nodal injection to the net active-power flow in line (m, n). The parametrization of voltage magnitudes and phases with respect to k is dropped in (9)–(11) to contain notational burden. Note that while $P_{(m,n),[k]}$ is linearly related to nodal active- and reactive-power injections $P_{[k]}$ and $Q_{[k]}$, (8) is nonlinear in $|V|$ and θ. The expression in (5) follows straightforwardly by linearizing (8) around the operating point at time instant k. We refer readers to [21] for more details on this derivation.

2) Measurement-Based Sensitivities: In the above, the computation of line-flow sensitivity factors $\Phi_{(m,n),[k]}$ requires accurate and up-to-date network topology, parameters, and operating point information, which may not be available in real time. On the other hand, phasor measurement units (PMUs), which provide synchronized voltage, current, and frequency measurements as many as 60 times per second [22], enable one to estimate the line-flow sensitivities *without* an up-to-date system network model. To this end, assume measurements of $P_{(m,n),[k]}$ are available from PMUs, and collect incremental variations $\Delta P_{(m,n),[k]} = P_{(m,n),[k+1]} - P_{(m,n),[k]}$, $k = 1, \ldots, \eta + 1$, into vector $\Delta \Pi_{(m,n)} \in \mathbb{R}^\eta$, i.e., $\Delta \Pi_{(m,n)} = [\Delta P_{(m,n),[1]}, \ldots, \Delta P_{(m,n),[\eta]}]^\mathrm{T}$. Similarly, collect PMU measurements of variations in active-power injections $\Delta P_{[k]}$, $k = 1, \ldots, \eta$, into matrix $\Delta \Pi \in \mathbb{R}^{\eta \times |\mathcal{N}|}$, i.e., $\Delta \Pi = [\Delta P_{[1]}, \ldots, \Delta P_{[\eta]}]^\mathrm{T}$. Then, it follows that [23]

$$\Delta \Pi_{(m,n)} = \Delta \Pi \Phi_{(m,n)}^\mathrm{T} + e_{(m,n)}, \tag{12}$$

where $e_{(m,n)}$ accounts for mismatches resulting from the active- and reactive-power decoupling assumption as well as measurement errors. If $\eta > |\mathcal{N}|$, then (12) is an overdetermined system. With weighted least-squares (WLS) estimation, the solution for $\Phi_{(m,n)}$ is given by [23]

$$\Phi_{(m,n)}^\mathrm{T} = (\Delta \Pi^\mathrm{T} W \Delta \Pi)^{-1} \Delta \Pi^\mathrm{T} W \Delta \Pi_{(m,n)}, \tag{13}$$

where $W \in \mathbb{R}^{\eta \times \eta}$ is a weighing matrix. In the generic WLS method with uncorrelated measurement errors, W is a diagonal matrix, and the more recent measurements are preferentially weighted by setting $[W]_{ii} = \varphi^{\eta - i}$ for some fixed "forgetting" factor $\varphi \in (0, 1]$ [24]. The formulation in (13) implies that all buses are equipped with PMUs. To relax this, consider the intuition that most line flows are significantly affected by only a small set of electrically nearby buses [25]. In Section V, this intuition is verified via simulations when the desired control objective is achieved by using only measurements from buses selected in a sparsity-promoting controller structure (which is detailed in Section IV). In these cases, the number of columns in $\Delta \Pi$ is less than $|\mathcal{N}|$. As a result, fewer sets of measurements

would be needed to solve the WLS problem in (13), thereby reducing its computational burden.

D. System Dynamical Models

As mentioned in Section II-C, we are interested in controlling the active-power flows on E transmission lines of interest, while ensuring zero steady-state frequency offset. We first consider dynamics arising from frequency deviations of synchronous generators, and then unwrap (5) to obtain synthetic line-flow dynamics.

1) Synchronous Generator Dynamics: For generator i, let ω_i and P_i^{m} denote the rotor electrical angular speed and the mechanical power, respectively. Pertinent dynamics of generator i are given by

$$M_i \dot{\omega}_i = P_i^{\mathrm{m}} - P_i^{\mathrm{e}} - D_i \left(\omega_i - \omega_{\mathrm{s}} \right), \qquad (14)$$

$$\tau_i \dot{P}_i^{\mathrm{m}} = -P_i^{\mathrm{m}} + P_i^{\mathrm{r}} - R_i^{-1} \left(\omega_i - \omega_{\mathrm{s}} \right), \qquad (15)$$

where M_i, D_i, and P_i^{e} are, respectively, the inertia constant, damping coefficient, and electrical power output of generator i; τ_i, P_i^{r}, and R_i denote the governor time constant, reference power input, and droop constant, respectively; and ω_{s} represents the synchronous rotating speed.

Next, we consider perturbations in ω_i and P_i^{m} away from a steady-state operating point. For the set of synchronous generators $\mathcal{G}$, collect variations in the synchronous-generator frequencies and mechanical power state vectors into $\Delta \omega = [\Delta \omega_1, \ldots, \Delta \omega_{|\mathcal{G}|}]^{\mathrm{T}}$ and $\Delta P^{\mathrm{m}} = [\Delta P_1^{\mathrm{m}}, \ldots, \Delta P_{|\mathcal{G}|}^{\mathrm{m}}]^{\mathrm{T}}$, respectively. Similarly, collect the variations in generator electrical power and reference power inputs into vectors $\Delta P^{\mathrm{e}} = [\Delta P_1^{\mathrm{e}}, \ldots, \Delta P_{|\mathcal{G}|}^{\mathrm{e}}]^{\mathrm{T}}$ and $\Delta P_{\mathcal{G}} = [\Delta P_1^{\mathrm{r}}, \ldots, \Delta P_{|\mathcal{G}|}^{\mathrm{r}}]^{\mathrm{T}}$, respectively. Then, we can express the generator dynamics compactly in matrix form as

$$\begin{bmatrix} \Delta \dot{\omega} \\ \Delta \dot{P}^{\mathrm{m}} \end{bmatrix} = \begin{bmatrix} -MD & M \\ -\tau R & -\tau \end{bmatrix} \begin{bmatrix} \Delta \omega \\ \Delta P^{\mathrm{m}} \end{bmatrix} + \begin{bmatrix} \mathbb{0} \\ \tau \end{bmatrix} \Delta P_{\mathcal{G}} - \begin{bmatrix} M \\ \mathbb{0} \end{bmatrix} \Delta P^{\mathrm{e}},$$

$$=: \Sigma \begin{bmatrix} \Delta \omega \\ \Delta P^{\mathrm{m}} \end{bmatrix} + \Omega \Delta P_{\mathcal{G}} + \Theta \Delta P^{\mathrm{e}}, \qquad (16)$$

with M, D, τ, and R given by

$$M = \mathrm{diag}\left(M_1^{-1}, \ldots, M_{|\mathcal{G}|}^{-1} \right), \; D = \mathrm{diag}(D_1, \ldots, D_{|\mathcal{G}|}),$$

$$\tau = \mathrm{diag}\left(\tau_1^{-1}, \ldots, \tau_{|\mathcal{G}|}^{-1} \right), \; R = \mathrm{diag}(R_1^{-1}, \ldots, R_{|\mathcal{G}|}^{-1}),$$

and $\mathbb{0}$s are matrices of all zeros with appropriate dimension. Finally, we discretize the continuous-time synchronous generator dynamics in (16) and combine the resultant with line-flow dynamics described next.

2) Line-Flow Dynamics: Reorder entries of ΔP in (5) so that $\Delta P = [\Delta P_{\mathcal{G}}^{\mathrm{T}}, \Delta P_{\mathcal{L}}^{\mathrm{T}}]^{\mathrm{T}}$, where $\Delta P_{\mathcal{L}}$ collects variations in active-power injections at load buses; also reorder entries of $\Phi_{(m,n),[k]}$ in (5) accordingly. Then, collecting instances of (5) for E lines of interest (out of a total of $|\mathcal{E}|$ lines in the system), we obtain

$$\Delta F_{[k]} = \Phi_{[k]} \Delta P_{[k]} + \zeta_{[k]}, \qquad (17)$$
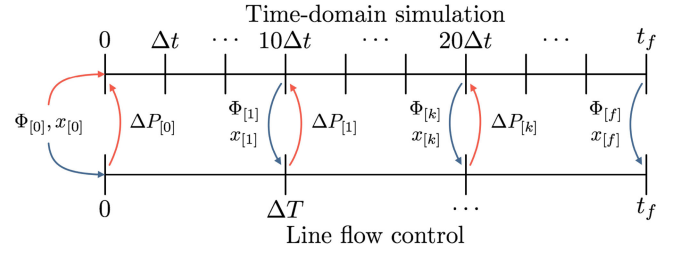
Fig. 1. Time evolution of information exchange between actual system dynamical response (generated via time-domain simulation of network differential-algebraic model) and line-flow controller. At each time instant k, the line-flow controller, which uses the system in (19), obtains measurements of states $x_{[k]}$ and provides actuation signals $\Delta P_{[k]}$. Simultaneously, the controller obtains updated sensitivities $\Phi_{[k]}$ (using either model- or measurement-based methods) to compute the next actuation signals $\Delta P_{[k+1]}$.

where $\Delta F \in \mathbb{R}^E$ collects the flow variations in the lines of interest, and $\Phi_{[k]} \in \mathbb{R}^{E \times |\mathcal{N}|}$ is constructed appropriately from (9) or (13). Now, by unwrapping (17), we arrive at the following recurrence relation:

$$F_{[k+1]} = F_{[k]} + \Phi_{[k]} \Delta P_{[k]} + \zeta_{[k]}. \qquad (18)$$

3) State-Space Model: Define state, input, disturbance, and output vectors as

$$x_{[k]} = [F_{[k]}^{\mathrm{T}}, \Delta \omega_{[k]}^{\mathrm{T}}, (\Delta P_{[k]}^{\mathrm{m}})^{\mathrm{T}}]^{\mathrm{T}}, \quad u_{[k]} = \Delta P_{[k]},$$

$$z_{[k]} = [\zeta_{[k]}^{\mathrm{T}}, (\Delta P_{[k]}^{\mathrm{e}})^{\mathrm{T}}]^{\mathrm{T}}, \quad y_{[k]} = [F_{[k]}^{\mathrm{T}}, \Delta \omega_{[k]}^{\mathrm{T}}]^{\mathrm{T}},$$

respectively. The discrete-time system state-space model can be expressed compactly as

$$x_{[k+1]} = A x_{[k]} + B_{[k]} u_{[k]} + B_z z_{[k]},$$

$$y_{[k]} = C x_{[k]} + \mu_{[k]}, \qquad (19)$$

where $\mu_{[k]} \in \mathbb{R}^{E+|\mathcal{G}|}$ is a bounded vector that captures measurement noise, and matrices A, $B_{[k]}$, B_z, and C are expressed as

$$A = \begin{bmatrix} I_E & \mathbb{0} \\ \mathbb{0} & \Sigma_d \end{bmatrix}, \; B_{[k]} = \begin{bmatrix} \Phi_{[k]} \\ [\Omega_d, \mathbb{0}] \end{bmatrix},$$

$$B_z = \begin{bmatrix} I_E & \mathbb{0} \\ \mathbb{0} & \Theta_d \end{bmatrix}, \; C = \begin{bmatrix} I_{E+|\mathcal{G}|} & \mathbb{0} \\ \mathbb{0} & \mathbb{0} \end{bmatrix},$$

with Σ_d, Ω_d, and Θ_d representing the discrete-time analogues of Σ, Ω, and Θ, respectively, from (16), and $\mathbb{0}$s denote matrices of all zeros with appropriate dimension. Note that the control input $u_{[k]} = \Delta P_{[k]}$ adjusts the electrical active-power injections for loads $P_{\mathcal{L}}$ and the governor speed control input $P_{\mathcal{G}}$ for synchronous generators. Fig. 1 illustrates interactions between the actual system and the system model in (19) to be used in the design and implementation of the controller that achieves optimal tracking. Although the model developed in (19) focuses on active-power flows, it is worth noting that we can easily incorporate a recurrence relation for reactive-power flows analogous to (18) into the system model in (19). Appending $\Delta Q_{[k]}$ into the control inputs, we can adjust reactive-power injections for controllable loads in order to regulate line reactive-power flows.

III. OPTIMAL CONTROLLER DESIGN

With the system description in (19) in place, we propose to use a linear-quadratic-Gaussian (LQG) controller to achieve optimal tracking of line active-power flows and regulate system frequency at the nominal value, so that as $k \to \infty$, $F_{[k]} = F^{\mathrm{ref}}$ and $\Delta \omega_{[k]} = 0$, all while contending with measurement noise and errors arising from active- and reactive-power coupling. The LQG controller is a combination of a linear-quadratic regulator (LQR) state feedback and a Kalman filter state estimator; we describe each component in detail next.

The LQR optimal feedback control law is

$$u_{[k]} = -K x_{[k]}, \tag{20}$$

where the state feedback $K \in \mathbb{R}^{|\mathcal{N}| \times (E+2|\mathcal{G}|)}$ (and in turn, $u_{[k]}$) is designed by solving [26]

$$\underset{K}{\text{minimize}} \ J(K) = \sum_{k=0}^{\infty} \left(x_{[k]}^{\mathrm{T}} \Psi_x x_{[k]} + u_{[k]}^{\mathrm{T}} \Psi_u u_{[k]} \right). \tag{21}$$

In (21), $\Psi_x \in \mathbb{R}^{(E+2|\mathcal{G}|) \times (E+2|\mathcal{G}|)}$ ($\Psi_x = \Psi_x^{\mathrm{T}}$, $\Psi_x \succeq 0$) and $\Psi_u \in \mathbb{R}^{|\mathcal{N}| \times |\mathcal{N}|}$ ($\Psi_u = \Psi_u^{\mathrm{T}}$, $\Psi_u \succ 0$) are performance-index weighing matrices. Namely, Ψ_x specifies the cost of line active-power flows and synchronous generator frequencies deviating away from their desired reference values, and entries of Ψ_u embed the costs of the control inputs. In our setting, control inputs are nodal injections arising from either generators or controllable loads, i.e., those with adjustable active-power set points. Fixed loads are ascribed greater cost in Ψ_u such that their corresponding set points remain unchanged.

Remark 1 (Incorporating Capacity Limits): To ensure that the controller respects capacity limits on generator or controllable-load injections, we may design entries of Ψ_u as follows. Given the maximum acceptable injection variation away from the current operating point, denoted by ΔP^{max}, Ψ_u would be a diagonal matrix expressed as [27]

$$\Psi_u = \mathrm{diag} \left(\frac{\mathbb{1}_{|\mathcal{N}|}}{\Delta P^{\mathrm{max}} \circ \Delta P^{\mathrm{max}}} \right). \tag{22}$$

■

In accordance with standard LQR design, the optimal state feedback is given by [26]

$$K = \left(\Psi_u + B_{[k]}^{\mathrm{T}} G B_{[k]} \right)^{-1} B_{[k]}^{\mathrm{T}} G A, \tag{23}$$

where G is the unique positive-definite solution of the discrete-time algebraic Riccati equation (DARE) described by [26]

$$G = A^{\mathrm{T}} G A - A^{\mathrm{T}} G B_{[k]} (\Psi_u + B_{[k]}^{\mathrm{T}} G B_{[k]})^{-1} B_{[k]}^{\mathrm{T}} G A + \Psi_x.$$

While (23) can be solved at each time instant k, in practical implementations, K would be updated periodically as the operating point sufficiently deviates from the previous one at which it was obtained. In fact, through extensive numerical case studies conducted for IEEE test systems, we find that the feedback obtained using the contributions of each active-power nodal injection to the line active-power flows at the initial condition is sufficient to track line flows to desired quantities. Thus, for all case studies in the remainder of the paper, we compute K only
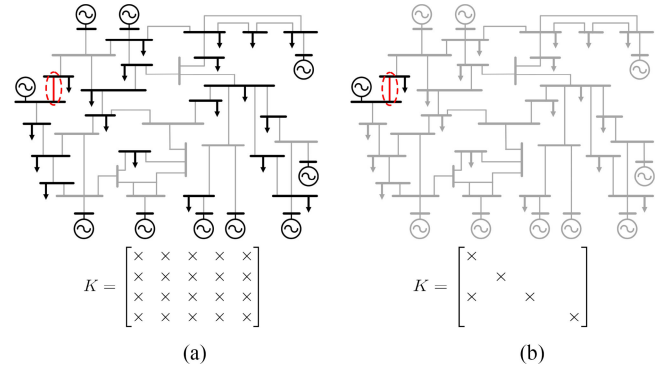
Fig. 2. Desired line flow to be controlled (encircled) and injections selected by controllers (dark trace). (a) For $\gamma = 0$, the optimal feedback K is dense and the controller tends to use all injections in the network. (b) With $\gamma > 0$, the optimal controller design yields a sparse K and uses only a subset of buses at the expense of closed-loop performance degradation.

once using $B_{[0]}$ in (23), i.e., the controller is designed using the line-flow sensitivities computed at the initial steady state.

To contend with measurement noise $\mu_{[k]}$, a state estimator is established as follows:

$$\widehat{x}_{[k+1]} = A \widehat{x}_{[k]} + B_{[k]} u_{[k]} + \Gamma \left(y_{[k]} - C \widehat{x}_{[k]} \right), \tag{24}$$

where $\widehat{x}_{[k]}$ represents the state estimates and Γ is the steady-state optimal Kalman filter gain, given by [26]

$$\Gamma = A O C^{\mathrm{T}} \left(C O C^{\mathrm{T}} + R_\mu \right)^{-1}. \tag{25}$$

In (25), R_μ denotes the measurement noise (i.e., $\mu[k]$) covariance, and O is the unique positive definite solution for the Kalman filter DARE [26]

$$O = A O A^{\mathrm{T}} + R_z - A O C^{\mathrm{T}} \left(R_\mu + C O C^{\mathrm{T}} \right)^{-1} C O A^{\mathrm{T}},$$

where R_z denotes the covariance of $z_{[k]}$. Based on the separation principle, the LQR state feedback control law and Kalman filter observer are designed separately and combined afterwards [26].

In general, the problem in (21) yields a dense state feedback matrix K, as shown in Fig. 2(a), which implies that a centralized controller must be able to vary injections at all buses in the system. Since such an assumption may not be practical for a large-scale power system, next, we relax these requirements and propose to use a sparsity-promoting optimal controller that uses injections from only a subset of buses (usually electrically near the lines of interest), as motivated in Fig. 2(b).

IV. SPARSITY-PROMOTING OPTIMAL CONTROL

In this section, we extend the continuous-time ADMM algorithm in [14] that identifies desirable controller sparsity patterns to our discrete-time problem setting.

A. Problem Formulation

The objective is to design the optimal state feedback matrix K, subject to structural constraints that dictate the locations of nonzero entries in K. With the subspace $\mathcal{S}$ embodying these

constraints, we search for stabilizing K that optimizes [14]

$$\underset{K}{\text{minimize}} \quad J(K)$$

$$\text{subject to} \quad K \in \mathcal{S}, \tag{26}$$

where $J(K)$ is the LQR quadratic cost function in (21). In the absence of structural constraints on K, the solution to (26) reduces to that of the LQR problem in (21), which generally yields a dense feedback matrix. Solving (26) becomes combinatorially intractable as the dimension of K grows. So instead, consider an optimization scheme that penalizes the ℓ_1-norm of the feedback matrix, as follows [14]:

$$\underset{\widetilde{K}}{\text{minimize}} \quad J(\widetilde{K}) + \gamma g(\widetilde{K}). \tag{27}$$

In (27), $g(\widetilde{K})$ represents a sparsity-promoting penalty function, which can be expressed as the weighted ℓ_1-norm of $\widetilde{K}$

$$g(\widetilde{K}) = \sum_{i,j} W_{ij} |[\widetilde{K}]_{ij}|, \tag{28}$$

where weights $W_{ij} \geq 0$. By incorporating $g(\widetilde{K})$ into the optimization problem, the structural constraint imposed on $\widetilde{K}$ in (26) is eliminated. The positive scalar γ emphasizes the sparsity level of $\widetilde{K}$, i.e., larger γ promotes sparser $\widetilde{K}$, while $\gamma = 0$ recovers the non-sparse feedback in (23) obtained by solving (21). Starting from this initial value, an iterative algorithm—ADMM—is employed to solve (27) for different and increasingly larger values of γ. Subsequently, the value of γ is chosen based on the trade-off between the closed-loop $\mathcal{H}_2$ performance (i.e., value of J) and the sparsity of $\widetilde{K}$. Finally, the sparsity pattern is fixed and the optimal structured state feedback is obtained by solving the original problem in (26). Fig. 2 illustrates the effect of γ on the sparsity of K and consequently the required control inputs: $\gamma = 0$ leads to dense K, while $\gamma > 0$ promotes sparser K.

B. Identifying Sparsity Patterns Via ADMM

We extend the setting in [14] to the discrete-time case and identify favourable sparsity patterns using ADMM. The ADMM algorithm exploits the separability of the sparsity-promoting penalty function g and the differentiability of J. The introduction of an additional variable Z and an additional constraint $\widetilde{K} - Z = \mathbb{0}$ facilitate the decoupling of (27) into two parts that depend on two different variables [14]. Consider the following constrained optimization problem

$$\underset{\widetilde{K}}{\text{minimize}} \quad J(\widetilde{K}) + \gamma g(Z)$$

$$\text{subject to} \quad \widetilde{K} - Z = \mathbb{0}, \tag{29}$$

which is equivalent to the problem in (27). The augmented Lagrangian associated with (29) is given by [14]

$$\mathcal{L}_\rho(\widetilde{K}, Z, \Lambda) = J(\widetilde{K}) + \gamma g(Z) + \text{Tr}\{\Lambda^{\text{T}}(\widetilde{K} - Z)\}$$

$$+ \frac{\rho}{2} \|\widetilde{K} - Z\|_{\text{F}}^2, \tag{30}$$

where Λ is the matrix of Lagrange multipliers and ρ is a positive scalar. The ADMM algorithm uses a sequence of iterations to

search for a minimizer in (29) as follows [14]:

$$\widetilde{K}^{\ell+1} := \arg\min_{\widetilde{K}} \mathcal{L}_\rho(\widetilde{K}, Z^\ell, \Lambda^\ell) \tag{31}$$

$$Z^{\ell+1} := \arg\min_{Z} \mathcal{L}_\rho(\widetilde{K}^{\ell+1}, Z, \Lambda^\ell) \tag{32}$$

$$\Lambda^{\ell+1} := \Lambda^\ell + \rho(\widetilde{K}^{\ell+1} - Z^{\ell+1}) \tag{33}$$

until $\|\widetilde{K}^{\ell+1} - Z^{\ell+1}\|_{\text{F}} \leq \epsilon$ and $\|Z^{\ell+1} - Z^\ell\|_{\text{F}} \leq \epsilon$, with initial conditions $\widetilde{K}^0$ obtained from (23), $Z^0 = \widetilde{K}^0$, and $\Lambda^0 = \mathbb{0}$, and $\epsilon > 0$ is a predefined tolerance for the equality constraint in (29).

The first step in the ADMM algorithm is to solve the $\widetilde{K}$-minimization problem in (31). The first-order necessary condition of optimality with respect to $\widetilde{K}$ is

$$\mathbb{0} = \nabla_{\widetilde{K}} \mathcal{L}_\rho(\widetilde{K}, Z^\ell, \Lambda^\ell) = \nabla J(\widetilde{K}) + \Lambda^\ell + \rho(\widetilde{K} - Z^\ell), \tag{34}$$

where the gradient of J is given by

$$\nabla J(\widetilde{K}) = 2(\Psi_u \widetilde{K} - B^{\text{T}} G(A - B\widetilde{K}))L, \tag{35}$$

with L and G being the controllability and observability Gramians of the closed-loop system, which are obtained as the solutions of

$$(A - B\widetilde{K})L(A - B\widetilde{K})^{\text{T}} - L = -B_z B_z^{\text{T}}, \tag{36}$$

$$(A - B\widetilde{K})^{\text{T}} G(A - B\widetilde{K}) - G = -\Psi_x - \widetilde{K}^{\text{T}} \Psi_u \widetilde{K}. \tag{37}$$

The derivation of (35) is provided in Appendix B. The update $\widetilde{K}^{\ell+1}$ is obtained via the Anderson-Moore method, which proceeds as follows. First, with $\widetilde{K}$ fixed to the value $\widetilde{K}^\ell$ in (36)–(37), they are solved to obtain L and G. Then, the solved L and G are substituted into (35), and the resultant into (34), which is solved to yield $\widetilde{K} = \overline{K}^\ell$. Subsequently, the update $\widetilde{K}^{\ell+1} = \widetilde{K}^\ell + s^\ell(\overline{K}^\ell - \widetilde{K}^\ell)$, where s^ℓ is a step size determined by the Armijo rule [28]. In the update, $\overline{K}^\ell - \widetilde{K}^\ell$ forms a descent direction of (34), which can be exploited by line search methods to determine a suitable step size [14].

With the $\widetilde{K}^{\ell+1}$ update in hand, the next step is to solve (32). Setting $\nabla \mathcal{L}_\rho(\widetilde{K}^{\ell+1}, Z, \Lambda^\ell)$ to zero yields the first-order necessary condition for optimality with respect to Z:

$$\mathbb{0} = \gamma \nabla g(Z) - \Lambda^\ell - \rho(\widetilde{K}^{\ell+1} - Z). \tag{38}$$

Since g can be written as a summation of component-wise functions of Z, decompose (38) into subproblems that involve scalar variables $[Z]_{ij}$. This way, in solving (38), the entry-wise Z-update is given by

$$[Z]_{ij}^{\ell+1} = \begin{cases} \left(1 - \frac{a}{|\sigma_{ij}^\ell|}\right) \sigma_{ij}^\ell, & |\sigma_{ij}^\ell| > a \\ 0, & |\sigma_{ij}^\ell| \leq a, \end{cases} \tag{39}$$

where $\sigma^\ell = \rho^{-1} \Lambda^\ell + \widetilde{K}^{\ell+1}$ and $a = \gamma \rho^{-1} W_{ij}$. The derivation of (39) is provided in Appendix C. Using (39), entries $[Z]_{ij}^{\ell+1}$ can be aggressively driven to zero by increasing γ and W_{ij} and by decreasing ρ. Finally, in each iteration, the updated $\Lambda^{\ell+1}$ is obtained via (33) with $\widetilde{K}^{\ell+1}$ and $Z^{\ell+1}$. The ADMM iterations continue until the stopping criteria are satisfied with optimizers given by $\widetilde{K}^\star$, $Z^\star$, and $\Lambda^\star$. This procedure is summarized in Algorithm 1.

Algorithm 1: Identify Sparsity Patterns via ADMM.

Input: K for standard LQR problem computed via (23), scalar parameter γ, and predefined threshold ϵ.

Output: Sparse feedback matrix $\widetilde{K}^\star$ that optimizes (27).

1: **Initialize.** Set $\widetilde{K}^0 = K$, $Z^0 = \widetilde{K}^0$, $\Lambda^0 = \mathbb{0}$, and counter $\ell = -1$.
2: **repeat**
3:     Set $\ell \leftarrow \ell + 1$
4:     Solve (36) and (37) with $\widetilde{K} = \widetilde{K}^\ell$ to obtain L and G
5:     Substitute L and G into (34) to obtain $\overline{K}^\ell$
6:     Update $\widetilde{K}^{\ell+1} = \widetilde{K}^\ell + s^\ell(\overline{K}^\ell - \widetilde{K}^\ell)$
7:     Update $Z^{\ell+1}$ using (39) and $\Lambda^{\ell+1}$ using (33)
8: **until** $||\widetilde{K}^{\ell+1} - Z^{\ell+1}||_F \le \epsilon$ and $||Z^{\ell+1} - Z^\ell||_F \le \epsilon$

Algorithm 2: Structurally Constrained Optimal Feedback.

Input: $\widetilde{K}^\star \in \mathcal{S}$ obtained from Algorithm 1 and predefined threshold ϵ.

Output: Sparse feedback matrix $K^\star \in \mathcal{S}$ that optimizes (26).

1: **Initialize.** Set $K^0 = \widetilde{K}^\star \in \mathcal{S}$ and counter $\ell = -1$.
2: **repeat**
3:     Set $\ell \leftarrow \ell + 1$
4:     Compute ΔK^ℓ that minimizes (41)
5:     Update $K^{\ell+1} = K^\ell + s^\ell \Delta K^\ell$
6: **until** $||\nabla J(K^{\ell+1})||_F \le \epsilon$

C. Solving the Structurally Constrained Problem in (26)

The ADMM algorithm outlined previously only identifies the desired sparsity pattern of K as that of $\widetilde{K}^\star \in \mathcal{S}$, which can be described by the structural identity

$$[I_\mathcal{S}]_{ij} = \begin{cases} 1, & \text{if } [\widetilde{K}^\star]_{ij} \ne 0, \\ 0, & \text{if } [\widetilde{K}^\star]_{ij} = 0. \end{cases} \quad (40)$$

With this desired pattern in hand, we return to the structurally constrained problem in (26) and solve it using descent algorithms such as Newton's method to obtain the optimal $K^\star \in \mathcal{S}$ that minimizes the original cost function in (21). Particularly, beginning with an initial feedback $K^0 = \widetilde{K}^\star \in \mathcal{S}$, the objective function is re-evaluated by updating K according to $K^{\ell+1} = K^\ell + s^\ell \Delta K^\ell$, until $||\nabla J(K^{\ell+1})||_F \le \epsilon$. In each iteration, s^ℓ is the step size, and $\Delta K^\ell \in \mathcal{S}$ is the Newton direction determined by the minimizer of the second-order approximation of the objective function in (21). Particularly, $\Delta K^\ell \in \mathcal{S}$ is the minimizer of

$$\big\langle \nabla J(K^\ell) \circ I_\mathcal{S}, \Delta K^\ell \big\rangle + \frac{1}{2} \big\langle H(K^\ell, \Delta K^\ell) \circ I_\mathcal{S}, \Delta K^\ell \big\rangle, \quad (41)$$

where $H(\cdot, \cdot)$ is the Hessian matrix of the objective function in (21). Note that pertinent entries in ΔK^ℓ are enforced to be zero via suitable entry-wise multiplication with $I_\mathcal{S}$. This procedure is summarized in Algorithm 2.
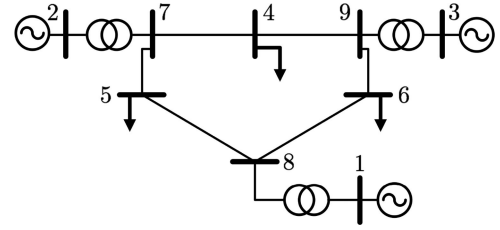
Fig. 3. Network topology for WECC 3-machine 9-bus system.
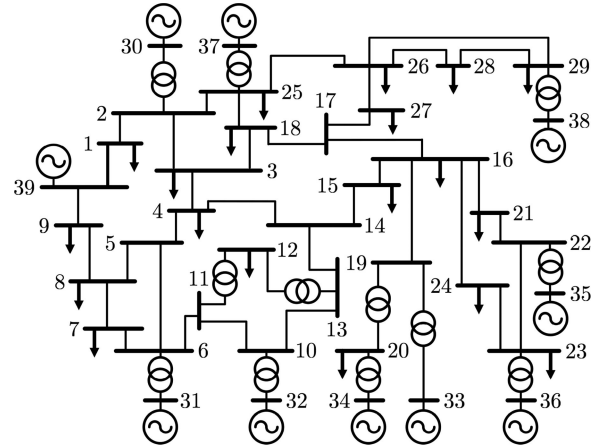
Fig. 4. Network topology for NE 10-machine 39-bus system.

V. CASE STUDIES

This section demonstrates the effectiveness of controllers presented in Sections III–IV via numerical case studies involving the Western Electricity Coordinating Council (WECC) 3-machine 9-bus and the New England (NE) 10-machine 39-bus test systems (see Figs. 3 and 4, respectively). The WECC case study illustrates the trade-off between controller sparsity and system closed-loop performance; and the NE case study demonstrates scalability of the proposed method. We also report execution times to design the controller in the WECC, the NE, and the Northeast Power Coordinating Council (NPCC) 48-machine 140-bus test systems [29]. Although a simplified model is used to design the LQG controllers, they are verified with time-domain simulations of a nonlinear differential-algebraic model that includes dynamics arising from two-axis synchronous generators, governors, and exciters performed using PSAT [30]. Synthetic measurements are sampled from the PSAT simulation at discrete intervals of $\Delta T = 0.0333$ s, well within the capability of current measurement technology [22]. The proposed controller then synthesizes the appropriate actuation signals that feed back as inputs into the PSAT simulation as shown in Fig. 1. The controller design procedure used throughout this section is summarized in Fig. 5.

A. WECC Test System

In this case study, we wish to regulate the active-power flows in lines (9, 6) and (7, 5), which have initial steady-state flows of $P_{(9,6),[0]} = 0.608$ p.u. and $P_{(7,5),[0]} = 0.866$ p.u., respectively. However, we would like to reduce the flows on lines (9, 6) and
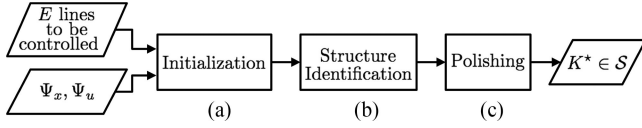
Fig. 5. Overall controller design procedure. (a) Initialization: assemble system model in (19) and compute dense feedback matrix K for standard LQR problem via (23). (b) Structure identification: identify desired sparsity pattern by solving (27) via Algorithm 1. (c) Polishing: compute optimal sparsity-promoting feedback matrix $K^\star \in \mathcal{S}$ by solving (26) via Algorithm 2.
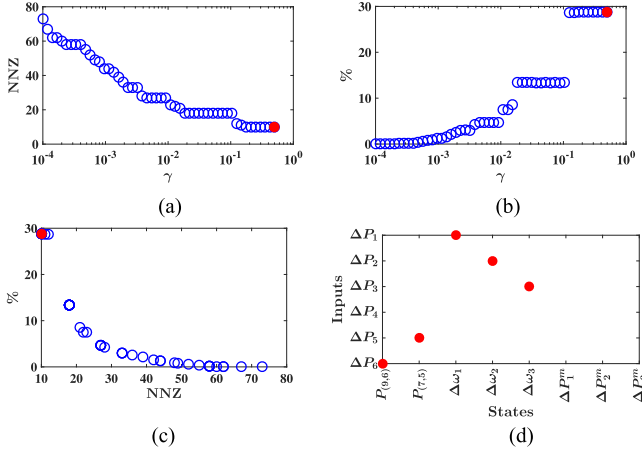
Fig. 6. WECC test system: sparsity-promoting algorithm performance evaluation. (a) Sensitivity of NNZ entries in feedback matrix to γ-value. (b) Sensitivity of performance degradation to γ-value. (c) Sensitivity of performance degradation to NNZ entries in feedback matrix. (d) Pattern of nonzero entries in sparse feedback matrix for the filled-circle case in (a)–(c).

Fig. 7. WECC test system: comparison of trajectories without vs. with line-flow control; in the case with line-flow control, the sparsity-promoting controller with sparsity pattern in Fig. 6(d) is used. (a) Active-power flows in the two lines of interest. (b) Center-of-inertia frequency deviations.

(7, 5) to 0.5 p.u. and 0.7 p.u., respectively, by specifying optimal injections via the ideas presented in Section IV.

1) Sparse Controller Structure: With γ-values ranging from $\gamma = 10^{-4}$ to $\gamma = 0.5$ in the sparsity-promoting objective function (27), optimal state feedback matrices with various levels of sparsity are obtained. As γ grows, the number of nonzero (NNZ) entries decreases, as shown in Fig. 6(a). Also, as shown in Fig. 6(b), the $\mathcal{H}_2$ performance (as quantified by the value of the objective function $J(K)$ resulting from different feedback matrices) degrades commensurately. In Fig. 6(c), we plot the tradeoff between the NNZ entries and the $\mathcal{H}_2$ performance degradation. As an example (marked by filled circles in Fig. 6), populating 10.4% of available entries in the feedback degrades performance by only 28.8% as compared to the full K. The structure of this particular sparse K is shown in Fig. 6(d). It is worth noting that, by examining the electrical distance between the lines of interest and buses in the network, the sparsity-promoting controller naturally selects electrically nearby buses. This is in accordance with the intuition that most line flows are significantly affected by only injections at electrically nearby buses.

2) Presence vs. Absence of Flow Control: In order to illustrate the advantage of the proposed controller, we compare the system response obtained with versus without line-flow control. Consider the WECC test system, with initial steady-state line active-power flows $P_{(9,6),[0]} = 0.608$ p.u. and $P_{(7,5),[0]} = 0.866$ p.u. At $t = 5$ s, the uncontrollable load at bus 4 decreases,

which causes a net injection change of $\Delta P_4 = 0.3$ p.u. Without flow control, as shown by the solid trace in Fig. 7(a), we observe that the active-power flows in lines $(9, 6)$ and $(7, 5)$ increase and may exceed their limits due to the load change. On the other hand, with line-flow control (see dashed trace in Fig. 7(a)), the flows converge to desired reference values of $P_{(9,6)}^{\text{ref}} = 0.5$ p.u. and $P_{(7,5)}^{\text{ref}} = 0.7$ p.u. Here, the flows are regulated using the sparsity-promoting controller, the sparsity pattern of which is shown in Fig. 6(d). Note that in both cases, we retain the frequency regulation feature of the controller, so the center-of-inertia (COI) frequency converges to the reference frequency $\omega_s = 1$ p.u. as shown in Fig. 7(b).

B. New England Test System

Synchronous generators are connected to buses 30 to 39; all constant-power loads are assumed to be controllable. Initial active-power flows on lines $(39, 1)$, $(11, 6)$, $(39, 9)$, $(23, 22)$, and $(29, 26)$ are $P_{(39,1),[0]} = 4.39$ p.u., $P_{(11,6),[0]} = 1.95$ p.u., $P_{(39,9),[0]} = 5.56$ p.u., $P_{(23,22),[0]} = 0.11$ p.u., and $P_{(29,26),[0]} = 1.90$ p.u., respectively.

1) Sparse Controller Structure: In this case study, we regulate active-power flows on a subset of lines and compare the time-domain dynamic response of the full and sparse feedback designs. Both designs utilize the same state- and control-performance weights as in Section V-A. Suppose that, instead of their initial steady-state values, desired flows on lines $(39, 1)$, $(11, 6)$, $(39, 9)$, $(23, 22)$, and $(29, 26)$ are $P_{(39,1)}^{\text{ref}} = 4.2$ p.u., $P_{(11,6)}^{\text{ref}} = 1.8$ p.u., $P_{(39,9)}^{\text{ref}} = 5.4$ p.u., $P_{(23,22)}^{\text{ref}} = 0.3$ p.u., and $P_{(29,26)}^{\text{ref}} = 2$ p.u., respectively. Using the initial power-flow solution, line-flow sensitivities are computed via (9), with which the optimal full and sparse feedback gains are determined by
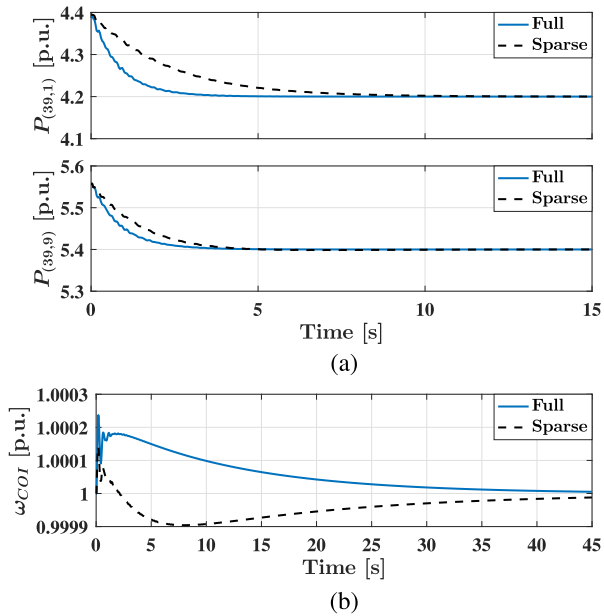
Fig. 8. NE test system: comparison of trajectories resulting from non-sparse vs. sparse feedback obtained as the solutions to (21) and (26), respectively, where the network topology remains fixed. (a) Active-power flows in two particular lines of interest. (b) Center-of-inertia frequency deviations.

Fig. 9. NE test system: comparison of trajectories resulting from using sparsity-promoting controller design where an undetected line outage occurs; line-flow sensitivities $\Phi_{[k]}$ are obtained with model- and sparse-measurement-based methods. (a) Active-power flows in two particular lines of interest. (b) Center-of-inertia frequency deviations.

solving (21) and (26), respectively. Similar to Section V-A, we assess the tradeoff between NNZ entries and performance degradation by varying γ in (27). Subsequent time-domain results are obtained by choosing $\gamma = 0.1$, which corresponds to 1.81% NNZ entries as compared to the full feedback matrix and 16.7% performance degradation.

The active-power flows on all lines converge to the desired reference values in both full and sparse feedback designs. In Fig. 8(a), we plot the line-flow trajectories for lines (39, 1) and (39, 9) until 15 s, which are representative of other lines. Additionally, the COI frequency in Fig. 8(b), converges to the reference frequency $\omega_s = 1$ p.u. with both controller designs.

2) Model-Based vs. Measurement-Based Sensitivities: Suppose line (8, 9) is disconnected at $t = 3$ s, but the offline model is not updated. Using the same sparse controller as before, we consider two ways to obtain sensitivities $\Phi_{[k]}$ at each time step in Fig. 1: (i) model-based computed via (9) at the initial operating point, (ii) measurement-based computed via (13) with up-to-date active-power injection measurements from only buses identified in the optimal sparsity pattern. In this way, (i) is restrictive as the offline model may not match the up-to-date topology and operating point. On the other hand, (ii) adapts to system changes and does not require any additional communication links beyond those needed for actuation by the sparse controller.

The line active-power flows depicted in Fig. 9(a) converge to their desired reference values despite the fault and topological modification. However, since the model-based approach does not update with the topological change, the sparse measurement-based estimation approach is more resilient to the disturbance. Moreover, the COI frequency depicted in Fig. 9(b) converges to the desired synchronous frequency $\omega_s = 1$ p.u. with
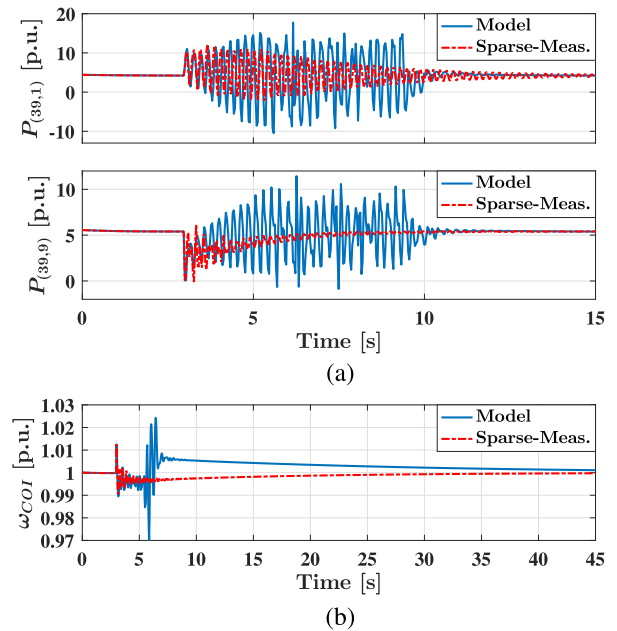
considerably lower fluctuations when the controller is used with the sparse measurement-based sensitivities.

C. Execution Times

To gauge the computational complexity of controller synthesis, we measure the running times required to execute the initialization, structure identification, and polishing steps (see Fig. 5) for the WECC, NE, and NPCC test systems. All algorithms are run using MATLAB R2017a on a MacBook Pro machine with 2.5 GHz quad-core Intel Core i7 processor, Turbo Boost up to 3.7 GHz, and 16 GB RAM. Execution times are reported in Table I. We note that structure identification via ADMM is the most time consuming step. In practice, we envision ADMM to be solved *offline* to identify the subset of injections to be used to control the line flows of interest. This sparsity structure may be updated periodically as the system sufficiently deviates from the previous operating point.

TABLE I
EXECUTION TIMES [S] FOR CONTROLLER DESIGN PROCEDURE,
CORRESPONDING TO STEPS OUTLINED IN FIG. 5: (A) INITIALIZATION,
(B) STRUCTURE IDENTIFICATION VIA ALGORITHM 1, AND
(C) POLISHING VIA ALGORITHM 2

	WECC 9-bus	NE 39-bus	NPCC 140-bus
Initialization	0.00166	0.00846	0.158
Structure Identification	0.321	2.49	12.5
Polishing	0.0173	0.0732	1.24
Total	0.340	2.57	13.9

VI. Concluding Remarks

In this paper, we proposed a method for regulating line active-power flows to desired setpoints while maintaining the nominal system frequency using sparsity-promoting control. The main advantages of the proposed control strategy are that it leverages existing resources, requires only local actuation commands, and adapts to potential network-topology and operating-point changes. The proposed controller time-domain dynamic performance was demonstrated via numerous case studies involving the WECC and New England test systems. Applicability of sparse measurement-based estimation of line-flow sensitivities with faults and line-outage contingencies were presented. Compelling avenues for future work include extending the developed framework to incorporate voltage regulation, uncertainty from uncontrollable generation, and communication failures. Another pertinent future direction is to formulate appropriate models for and to investigate the efficacy of output-feedback control designs.

Appendix

A. List of Abbreviations

ADMM   Alternating direction method of multipliers
AGC   Automatic generation control
COI   Center-of-inertia
DARE   Discrete algebraic Riccati equation
DER   Distributed energy resource
LQG   Linear quadratic Gaussian
LQR   Linear quadratic regulator
NE   New England
NNZ   Number of nonzero
NPCC   Northeast Power Coordinating Council
PMU   Phasor measurement unit
PSAT   Power System Analysis Toolbox
WECC   Western Electricity Coordinating Council
WLS   Weighted least squares

B. Derivation of $\nabla J(K)$ in (35)

To facilitate the derivation, we note that another way to express the objective function in (21), for stabilizing K, is [31]

$$J(K) = \text{Tr}\left\{B_z^{\text{T}} G(K) B_z\right\} = \text{Tr}\{G(K) B_z B_z^{\text{T}}\}, \qquad (42)$$

where the second equality above results from the cyclic permutation property of traces. First-order Taylor-series expansion of (42) around the solution K and corresponding $G(K)$ yields

$$\text{Tr}\{\nabla J(K)^{\text{T}} \Delta K\} = \text{Tr}\{\Delta G(K) B_z B_z^{\text{T}}\}. \qquad (43)$$

Similarly, around the same solution, first-order Taylor-series expansion of (37) yields

$$\mathbb{0} = (A - BK)^{\text{T}} \Delta G(K)(A - BK) - \Delta G(K)$$
$$+ \Delta K^{\text{T}}(\Psi_u K - B^{\text{T}} G(A - BK))$$
$$+ (\Psi_u K - B^{\text{T}} G(A - BK))^{\text{T}} \Delta K, \qquad (44)$$

where G and Ψ_u are symmetric matrices. Now, let L be the solution to the Lyapunov equation in (36). Pre-multiply (36) by

$\Delta G(K)$ and take the trace of both sides to obtain

$$-\text{Tr}\{\Delta G(K) B_z B_z^{\text{T}}\} = \text{Tr}\{-\Delta G(K) L$$
$$+ \Delta G(K)(A - BK) L (A - BK)^{\text{T}}\}. \qquad (45)$$

Post-multiply (44) by L and take the trace of both sides to get

$$0 = \text{Tr}\{(A - BK)^{\text{T}} \Delta G(K)(A - BK) L - \Delta G(K) L\}$$
$$+ \text{Tr}\{\Delta K^{\text{T}}(\Psi_u K - B^{\text{T}} G(A - BK)) L\}$$
$$+ \text{Tr}\{(\Psi_u K - B^{\text{T}} G(A - BK))^{\text{T}} \Delta K L\}. \qquad (46)$$

Recognizing that the first term above is equivalent to the right-hand side of (45), and combining (43), (45), and (46) with appropriate use of properties of the trace, we get

$$\text{Tr}\{\nabla J(K)^{\text{T}} \Delta K\} = \text{Tr}\{2 \Delta K^{\text{T}}(\Psi_u K - B^{\text{T}} G(A - BK)) L\},$$

from which we extract the expression for the gradient of J as

$$\nabla J(K) = 2\left(\Psi_u K - B^{\text{T}} G(A - BK)\right) L.$$

C. Derivation of $[Z]_{ij}^{\ell+1}$ in (39)

The derivation follows by solving (38), which begins with differentiating $g(Z) = \sum_{i,j} W_{ij} |[Z]_{ij}|$ with respect to each entry $[Z]_{ij}$ to get

$$\frac{\partial g(Z)}{\partial [Z]_{ij}} = \begin{cases} W_{ij}, & \text{if } [Z]_{ij} > 0, \\ -W_{ij}, & \text{if } [Z]_{ij} < 0, \\ \text{does not exist}, & \text{otherwise.} \end{cases}$$

Substituting the above back into (38), and defining $\sigma^\ell = \rho^{-1} \Lambda^\ell + \tilde{K}^{\ell+1}$ and $a = \gamma \rho^{-1} W_{ij}$, we obtain the entry-wise Z-update as

$$[Z]_{ij}^{\ell+1} = \begin{cases} -a + \sigma_{ij}^\ell, & \sigma_{ij}^\ell > a, \\ a + \sigma_{ij}^\ell, & \sigma_{ij}^\ell < -a, \\ 0, & \text{otherwise,} \end{cases}$$

which is equivalent to (39).

References

[1] S. Ahmad *et al.*, "Implementation of fuzzy unified power flow controller to control power flow dynamically in transmission line," in *Proc. Int. Conf. Adv. Elect. Eng.*, Dec. 2015, pp. 271–275.

[2] S. R. Gaigowal and M. M. Renge, "Distributed power flow controller using single phase DSSC to realize active power flow control through transmission line," in *Proc. Int. Conf. Comput. Power, Energy Inf., Commun.*, Apr. 2016, pp. 747–751.

[3] M. Andreasson, D. V. Dimarogonas, H. Sandberg, and K. H. Johansson, "Distributed control of networked dynamical systems: Static feedback, integral action and consensus," *IEEE Trans. Autom. Control*, vol. 59, no. 7, pp. 1750–1764, Jul. 2014.

[4] V. C. Gungor *et al.*, "Smart grid technologies: Communication technologies and standards," *IEEE Trans. Ind. Inf.*, vol. 7, no. 4, pp. 529–539, Nov. 2011.

[5] H. Singh, S. Hao, and A. Papalexopoulos, "Transmission congestion management in competitive electricity markets," *IEEE Trans. Power Syst.*, vol. 13, no. 2, pp. 672–680, May 1998.

[6] C. Zhao, E. Mallada, S. Low, and J. Bialek, "A unified framework for frequency control and congestion management," in *Proc. Power Syst. Comput. Conf.*, Jun. 2016, pp. 1–7.

[7] A. J. Wood and B. F. Wollenberg, *Power Generation, Operation, and Control*. New York, NY, USA: Wiley, 2012.

[8] P. McNamara and F. Milano, "Model predictive control-based AGC for multi-terminal HVDC-connected AC grids," *IEEE Trans. Power Syst.*, vol. 33, no. 1, pp. 1036–1048, Jan. 2018.

[9] Z. Yuan, S. W. H. d. Haan, J. B. Ferreira, and D. Cvoric, "A FACTS device: Distributed power-flow controller (DPFC)," *IEEE Trans. Power Electron.*, vol. 25, no. 10, pp. 2564–2572, Oct. 2010.

[10] D. M. Divan *et al.*, "A distributed static series compensator system for realizing active power flow control on existing power lines," *IEEE Trans. Power Del.*, vol. 22, no. 1, pp. 642–649, Jan. 2007.

[11] S. C. Müller, U. Häger, and C. Rehtanz, "A multiagent system for adaptive power flow control in electrical transmission systems," *IEEE Trans. Ind. Inf.*, vol. 10, no. 4, pp. 2290–2299, Nov. 2014.

[12] L. Gyugyi, "Unified power-flow control concept for flexible AC transmission systems," *Proc. Inst. Electr. Eng. C—Gener., Transmiss., Distrib.*, vol. 139, no. 4, pp. 323–331, Jul. 1992.

[13] A. Al-Digs, S. V. Dhople, and Y. C. Chen, "Linear-quadratic-Gaussian control of line active-power flow," in *Proc. IEEE Power Energy Soc. Gen. Meeting*, Jul. 2017, pp. 1–5.

[14] F. Lin, M. Fardad, and M. R. Jovanović, "Design of optimal sparse feedback gains via the alternating direction method of multipliers," *IEEE Trans. Autom. Control*, vol. 58, no. 9, pp. 2426–2431, Sep. 2013.

[15] F. Dörfler, M. R. Jovanović, M. Chertkov, and F. Bullo, "Sparsity-promoting optimal wide-area control of power networks," *IEEE Trans. Power Syst.*, vol. 29, no. 5, pp. 2281–2291, Sep. 2014.

[16] X. Wu, F. Dörfler, and M. R. Jovanović, "Input-output analysis and decentralized optimal control of inter-area oscillations in power systems," *IEEE Trans. Power Syst.*, vol. 31, no. 3, pp. 2434–2444, May 2016.

[17] A. Jain, A. Chakrabortty, and E. Biyik, "An online structurally constrained LQR design for damping oscillations in power system networks," in *Proc. Amer. Control Conf.*, May 2017, pp. 2093–2098.

[18] D. K. Molzahn *et al.*, "A survey of distributed optimization and control algorithms for electric power systems," *IEEE Trans. Smart Grid*, vol. 8, no. 6, pp. 2941–2962, Nov. 2017.

[19] J. Glover, M. Sarma, and T. Overbye, *Power System Analysis and Design*. Boston, MA, USA: Cengage Learning, 2008.

[20] Y. C. Chen and S. V. Dhople, "Power divider," *IEEE Trans. Power Syst.*, vol. 31, no. 6, pp. 5135–5143, Nov. 2016.

[21] Y. C. Chen, S. V. Dhople, A. D. Domínguez-García, and P. W. Sauer, "Generalized injection shift factors," *IEEE Trans. Smart Grid*, vol. 8, no. 5, pp. 2071–2080, Sep. 2017.

[22] "Steps to establish a real-time transmission monitoring system for transmission owners and operators within the eastern and western interconnections," US DOE & FERC, Washington, DC, USA, Feb. 2006. [Online]. Available: http://energy.gov/sites/prod/files/oeprod/DocumentsandMedia/final_1839.pdf

[23] Y. C. Chen, A. D. Domínguez-García, and P. W. Sauer, "Measurement-based estimation of linear sensitivity distribution factors and applications," *IEEE Trans. Power Syst.*, vol. 29, no. 3, pp. 1372–1382, May 2014.

[24] L. Ljung and T. Söderström, *Theory and Practice of Recursive Identification*. Cambridge, MA, USA: MIT Press, 1983.

[25] Y. C. Chen, A. D. Domínguez-García, and P. W. Sauer, "A sparse representation approach to online estimation of power system distribution factors," *IEEE Trans. Power Syst.*, vol. 30, no. 4, pp. 1727–1738, Jul. 2015.

[26] M. Athans, "The role and use of the stochastic linear-quadratic-Gaussian problem in control system design," *IEEE Trans. Autom. Control*, vol. AC-16, no. 6, pp. 529–552, Dec. 1971.

[27] G. Franklin, J. Powell, and E. A. Naeini, *Feedback Control of Dynamic Systems*. Englewood Cliffs, NJ, USA: Prentice-Hall, 2002.

[28] J. Nocedal and S. J. Wright, *Numerical Optimization*. Berlin, Germany: Springer-Verlag, 1999.

[29] J. H. Chow and K. W. Cheung, "A toolbox for power system dynamics and control engineering education and research," *IEEE Trans. Power Syst.*, vol. 7, no. 4, pp. 1559–1564, Nov. 1992.

[30] F. Milano, "An open source power system analysis toolbox," *IEEE Trans. Power Syst.*, vol. 20, no. 3, pp. 1199–1206, Aug. 2005.

[31] K. Zhou, J. C. Doyle, and K. Glover, *Robust and Optimal Control*. Upper Saddle River, NJ, USA: Prentice-Hall, 1996.

Abdullah Al-Digs (S'14) received the B.A.Sc. degree (with distinction) in electrical engineering from the University of British Columbia, Vancouver, BC, Canada, in 2015, where he is currently working toward the Ph.D. degree at the Department of Electrical and Computer Engineering. His research interests include power system analysis, operation, monitoring, and control.

Sairaj V. Dhople (M'13) received the B.S., M.S., and Ph.D. degrees in electrical engineering from the University of Illinois at Urbana-Champaign, Urbana, IL, USA, in 2007, 2009, and 2012, respectively. He is currently an Assistant Professor with the Department of Electrical and Computer Engineering, University of Minnesota, Minneapolis, MN, USA, where he is affiliated with the Power and Energy Systems Research Group. His research interests include modeling, analysis, and control of power electronics and power systems with a focus on renewable integration. He was the recipient of the National Science Foundation CAREER Award in 2015. He currently serves as an Associate Editor for the IEEE TRANSACTIONS ON ENERGY CONVERSION and the IEEE TRANSACTIONS ON POWER SYSTEMS.

Yu Christine Chen (S'10–M'15) received the B.A.Sc. degree in engineering science from the University of Toronto, Toronto, ON, Canada, in 2009, and the M.S. and Ph.D. degrees in electrical engineering from the University of Illinois at Urbana-Champaign, Urbana, IL, USA, in 2011 and 2014, respectively. She is currently an Assistant Professor with the Department of Electrical and Computer Engineering, The University of British Columbia, Vancouver, BC, Canada, where she is affiliated with the Electric Power and Energy Systems Group. Her research interests include power system analysis, monitoring, and control.